ADVANCED FUNCTIONAL MATERIALS
www.afm-journal.de

Surface Adaptive Dual-Layer Protection of Li-metal Anode for Extending Cycle-Life of Li–Sulfur Batteries with Lean Electrolyte

Bokyung Choi, Kyung-Geun Kim, Minhong Lim, Beomjun Kim, Jiyeon Seo, Jiwon Lee, Sanghyeon Park, Ki-Hyun Kim, Yong Min Lee, and Hongkyung Lee**

Building a lithium–sulfur (Li–S) battery with lean electrolytes is essential to far exceed the energy density of today's Li-ion. However, earlier electrolyte depletion triggered by Li-metal anodes (LMAs) causes sluggish Li–S redox kinetics and poor S utilization, resulting in a short cycle lifespan. To retard the electrolyte loss effectively, sustainable protection of LMAs is necessary against the dynamic interfacial evolution between LMA and protective layers (PLs). This study elucidates two critical parameters in securing the interfacial adaptivity of PLs upon local Li pitting: surface free energy (SFE) and Young's modulus through solid-mechanic simulations and experiments using three different PL models. To alleviate the PL delamination at the early stage, a dual-layer structured, adaptive protective layer (APL) is introduced to adapt the Li pitting-driven structural evolution of the PL|LMA interfaces. The APL consists of a high- SFE polymer as an inner layer, reducing the interfacial energy in contact with LMA surface, and a highly stretchable polymer for outer shield, serving as a physical barrier for the electrolyte and Li polysulfides. APL-coated LMA demonstrates stable cycling of Li–S cells, achieving a twofold extension of cycle-life compared to unprotected LMA, even superior to other single-layer PLs.

1. Introduction

Beyond the era of lithium (Li)-ion, Li–sulfur (Li–S) batteries have emerged as promising alternatives that surpass the specific energy limit of today's Li-ion. In addition to the merit of Li-metal anodes (LMAs), an elemental S (S_8) cathode features earth-abundance and high specific capacity (1675 mAh g^{-1}, delivering a high theoretical gravimetric energy density (2567 Wh kg^{-1}).[1–7] Indeed, Li–S cells that can achieve over 500 Wh kg^{-1} have been demonstrated in a practical cell format, which far exceeds the theoretical limit of the Li-ion cells (≈291 Wh kg^{-1}). One of the key milestones in practical Li–S cells is minimizing the electrolyte volume per S mass loading (E/S ratio).[8–12] Nonetheless, the practical energy density and cycling stability are not satisfactory yet, which makes it less competitive to today's Li-ion cells.[13–16]

Reducing the E/S ratio makes the cycling of Li–S cells more challenging.[17,18] Due to the intrinsic solution-based redox chemistry, soluble Li polysulfides (Li_2S_x, $2 < x \leq 8$, denotes as LiPS) intermediates can play a role in self-redox mediating. At a lower E/S ratio, the decrease in the LiPS dissolution causes sluggish S conversion kinetics, high polarization, and low S utilization.[19–23] In addition, the LMA-triggered intrinsic challenges, such as uncontrolled extensive growth of Li dendrites, inferior SEI stability, and irregular spatial/temporal evolution of electrolyte-LMA interface structure, have not been resolved yet,[24–26] inevitably resulting in ceaseless loss of Li inventory and electrolyte upon prolonged cycling. This series of LMA deterioration could be further exacerbated at low E/S ratio, where the dynamic change of electrolyte compositions and further reduction of the E/S ratio upon cycling, jointly leading to early failure of Li–S cell cycling.[27,28] Therefore, mediating the LMA reactivity against the electrolytes is prioritized to secure the long, stable cycling of practical Li–S batteries with lean electrolytes.

Building a protective layer (PL) onto the LMA surface has been revisited to overcome the above issues.[29–34] An ideal PL should possess excellent chemical/electrochemical stability, high Li^+ ion conductivity, and mechanical robustness to suppress the Li dendrite growth and the volume expansion of the LMA.[35]

B. Choi, M. Lim, B. Kim, J. Seo, J. Lee, S. Park, Y. M. Lee, H. Lee
Department of Energy Science and Engineering
Daegu Gyeongbuk Institute of Science and Technology (DGIST)
333 Techno Jungang-daero, Hyeonpung-eup, Dalseong-gun, Daegu 42988, Republic of Korea
E-mail: yongmin@yonsei.ac.kr; hongkyung.lee@dgist.ac.kr
K.-G. Kim, Y. M. Lee, H. Lee
Energy Science and Engineering Research Center
DGIST
333 Techno Jungang-daero, Hyeonpung-eup, Dalseong-gun, Daegu 42988, Republic of Korea
K.-H. Kim
Future Tech. Center
LG Energy Solution
30 Magokjungang 10-ro, Gangseo-gu, Seoul 07796, Republic of Korea
Y. M. Lee
Department of Chemical and Biomolecular Engineering
Yonsei University
50 Yonsei-ro, Seodaemun-gu, Seoul 03722, Republic of Korea
The ORCID identification number(s) for the author(s) of this article can be found under https://doi.org/10.1002/adfm.202316838

DOI: 10.1002/adfm.202316838

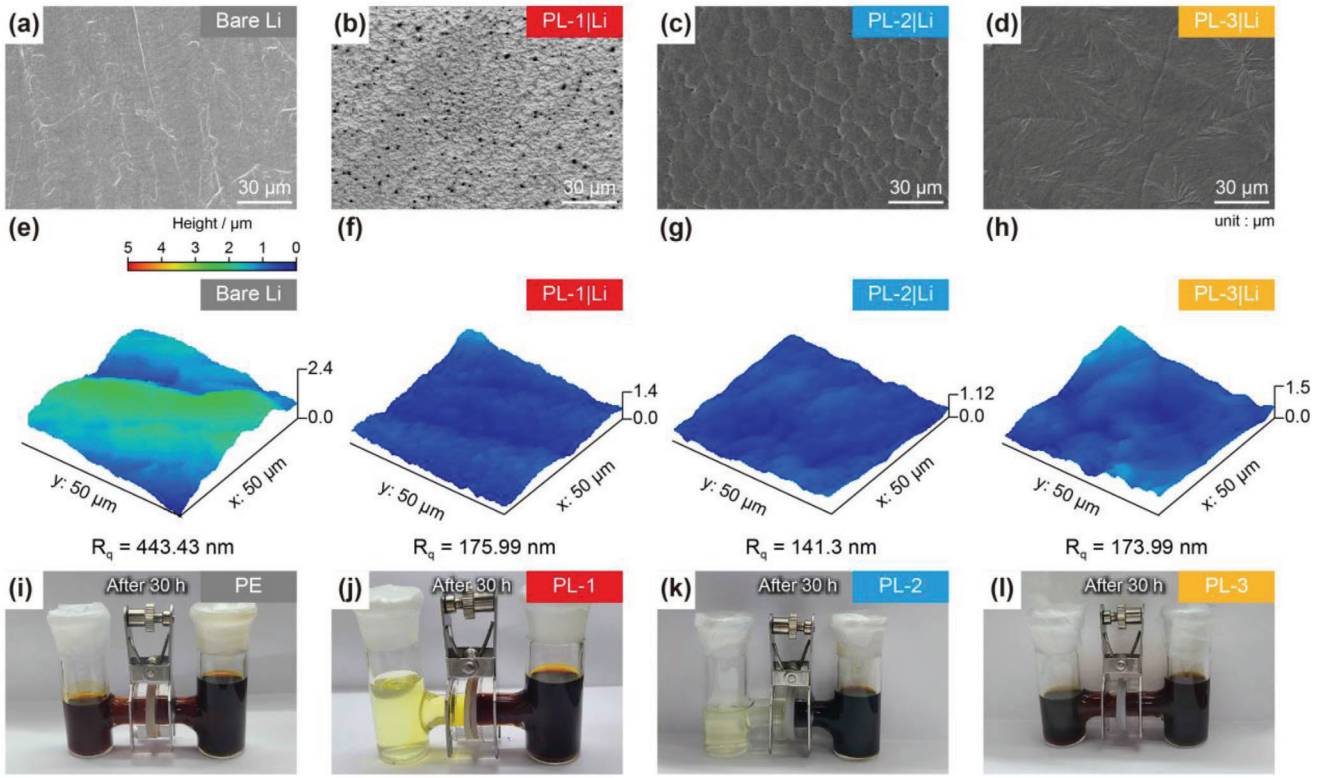

Figure 1. Morphology and structural characterization of the PL models. Top-view SEM images for a) bare Li, b) PL-1, c) PL-2, and d) PL-3, respectively. AFM-guided 3D surface topology images after coating PLs at 40 μm thick Li foil: e) bare Li, f) PL-1, g) PL-2, and h) PL-3, respectively. All samples are scanned 50 × 50 μm. LiPS diffusion test using H-type cell after 30 h i) PE, j) PL-1, k) PL-2, and l) PL-3.

Moreover, PLs should play an additional role in blocking the LiPS shuttle of the Li–S cells. Accordingly, numerous efforts for LMA protection have been devoted to exploiting the size-excluding materials[36–39] and ion perm-selective materials.[40–42] Despite the excellent LiPS rejection and improved cycling performances, the LMA protection can eventually fail by deteriorating the PL|LMA interface by Li stripping-initiated cycling of Li–S cells. Most commercial LMAs suffer from local pit dissolution, forming a huge cavity, thereby increasing the heterogeneity of the LMA surface.[43,44] Such irregular Li dissolution could cause a dynamic evolution of PL|LMA interfaces, leading to the failure of LMA protection. To secure the interfacial stability, a dual-layer PL (DPL) has been proposed by resembling the naturally formed SEI.[45,46] Nonetheless, the design factors for successful PL buildup in Li–S batteries are not fully established yet.

To gain insight into sustainable protection, this work unravels the failure scenarios of PLs, regarding the Li pitting-initiated structural evolution of PL|LMA interface. Owing to facile processibility and chemical/electrochemical stabilities,[47] polymers are primarily chosen as model PLs, including PVDF, PVDF-HFP, and PEO (PL-1, PL-2, and PL-3, respectively) to identify the PL-deterministic failure modes, such as delamination, penetration, and dissolution. The experimental results and simulation study suggested that securing the surface adaptivity of the PL is a prerequisite for sustainable LMA protection retarding electrolyte loss, which is crucial for the long stable cycling of Li–S cells with lean electrolytes. The surface adaptive DPL (APL), which features excellent adhesion and sufficient stretchability, was constructed by composing of a PEO inner layer, designed to reduce interfacial energy upon contact with LMA, and a PVDF-HFP outer shield, serving as a physical barrier for the LiPS and electrolyte. The APL can effectively mitigate the LiPS crossover and electrolyte decomposition, demonstrating a twofold longer cycle-life of Li–S cells with mildly lean electrolytes (5 μL mg^{-1}).

2. Results and Discussion

The cross-sectional SEM images reveal that all PLs were successfully coated with the same thickness (3 μm) (Figure S1a–d, Supporting Information). Although the naked-eye appearance of PLs looks similar, their surface microstructures were different as confirmed in SEM images (**Figure** 1a–d). Particularly, the PL-1 surface shows very small-sized protrusions and sporadic voids (black dots). On the other hand, PL-2 exhibits granule-like phase separations with a smoothened surface. Moreover, PL-3 exhibits a very large phase island. In the AFM study, the surface roughness decreased to ≈175 nm for PL-coated LMA, whereas 443.43 nm of bare Li, indicating that the PLs were well-coated, smoothing the original LMA surface (Figure 1e–h). A noticeable difference was grain size depending on the PL materials. While PL-1 and PL-2 exhibit a significantly smaller grain size, the largest grain size (>20 μm) was observed at the PL-3 (Figure S2a–d, Supporting Information). Such differences possibly originate from the interfacial compatibility between PL and LMA surfaces.

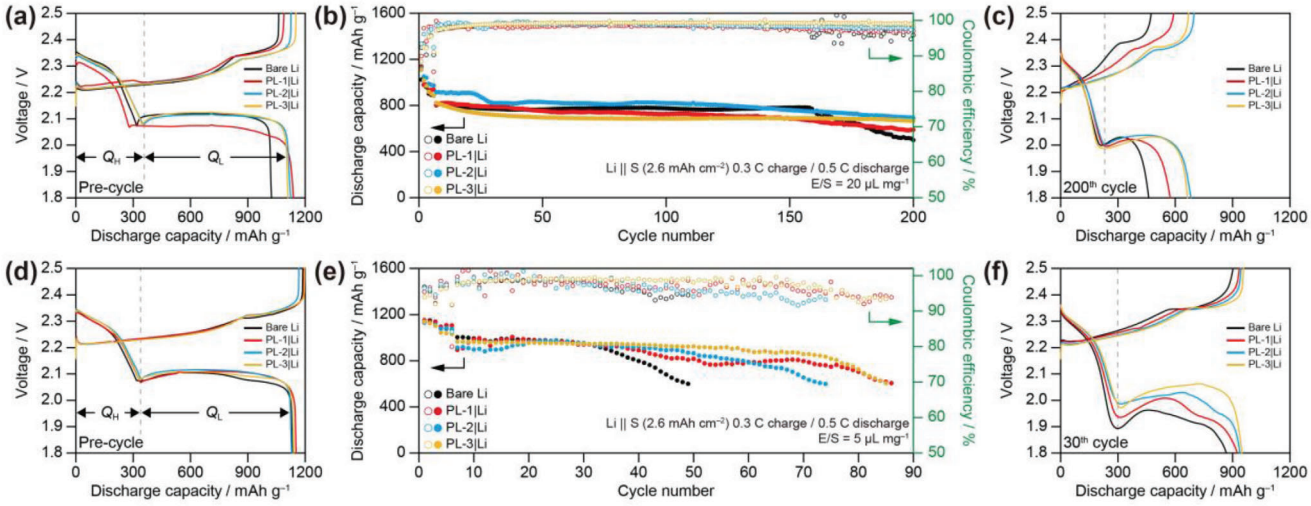

Figure 2. Cycling performance of Li–S full cells with different E/S ratios. a) Pre-cycle voltage profile for Li–S cells under flood electrolyte (E/S = 20 μL mg^{-1}). b) Cycle performance for Li–S cells under flooded electrolyte cycled at 0.3 C/0.5 C charge/discharge with bare Li, PL-1, PL-2, and PL-3. c) Voltage profiles for each Li–S cell after 200 cycles under flooded electrolyte. d) Pre-cycle voltage profiles for Li–S cells under lean electrolyte (E/S = 5 μL mg^{-1}). e) Cycle performance for Li–S cells cycled at 0.3 C/0.5 C charge/discharge with bare Li, PL-1, PL-2, and PL-3. f) The 30th voltage profile for Li–S cells under lean electrolyte.

As a physical barrier, the primary role of the PL coating is well-known to inhibit the detrimental reaction between LiPS and LMA. To assess this feature, H-shaped diffusion cells using dissolved LiPS (0.5 M Li_2S_6 in DOL/DME) were fabricated with different PLs (Figure S3, Supporting Information). While both PL-1 and PL-2 effectively suppressed LiPS crossover over 30 h, PL-3 was instantly swollen and allowed LiPS permeation within 1 h (Figure 1i–l). This implies that PL-3 may undergo partial dissolution in the ether-based electrolytes (Figure S4, Supporting Information), compromising its protective role.[48] Therefore, it is worth examining the cycling stability of Li–S full cells using PL-coated LMAs under flooded- and lean-electrolyte conditions to reveal that factor determines the cycling regarding interfacial compatibility and LiPS blocking.

The cycling of Li–S cells using bare Li and PL|LMAs was performed under flooded and lean electrolyte conditions. In the typical voltage profiles of Li–S cells, the higher voltage plateau (≈2.3 V) with the partial capacity (Q_H) is attributed to S_8 conversion to long-chain LiPS, while the lower voltage plateau (≈2.1 V) provides the remainder (Q_L) of total capacity, indicating to the conversion of Li_2S_4 to Li_2S.[49,50] With flooded electrolyte (E/S = 20 μL mg^{-1}), the cell with bare Li exhibited a relatively lower capacity (1024 mAh g^{-1}) and 92.4% of Coulombic efficiency (CE) during pre-cycle (**Figure 2a**), likely due to low S utilization. In contrast, the cells with PL-2 and PL-3 exhibited negligible overpotential increase and rendered a higher capacity (≈1124 mAh g^{-1}) and increased initial CE (≈93.4%), whereas the PL-1 cell showed a higher overpotential and slightly lower Q_H despite the LMA protection. As the cycling proceeded (Figure 2b), the bare Li cells failed earlier after 168 cycles (80% retention). The highest retention over 200 cycles was achieved by PL-2 (87.5%) that most effectively mitigated the LiPS crossover. Despite the capacity fading in the early stage, the PL-3 cell exhibited better capacity retention (84.3%) than the PL-1 cell (74%). As confirmed in Figure 2c, the PL-2 and PL-3 cells retained higher Q_L even compared to PL-1. The cell capacity retention is mostly related to the retention of Q_L capacity, which is mostly attributed to the precipitation of insulating Li_2S_2 and Li_2S onto the surfaces of both cathode and LMA.[51] The cycling of Li–S batteries with flood electrolytes is mainly affected by the effectiveness of Li protection in alleviating the S loss triggered by LiPS shuttle and side reactions with LMAs.

Interestingly, Li–S cell cycling at a lower E/S ratio (E/S = 5 μL mg^{-1}) shows a different trend from the previous results. While the voltage profiles were almost consistent at pre-cycle (Figure 2d), the maximum cycle numbers at 80% capacity retention were varied in order of PL-3 (70) ≈ PL-1 (70) > PL-2 (58) > bare Li (32) (Figure 2e). Nonetheless, PL-1 showed an unstable cycle behavior, showing a rapid capacity decay after 56 cycles, implying the PL degradation had already initiated earlier. The PL-3 demonstrated the best capacity retention even though it can adversely permit the LiPS permeation. The capacity retentions of cells with lean electrolytes can be correlated with overpotentials, particularly at the voltage valley, which reflects the extent of electrolyte loss during prolonged cycling (Figure 2f). The deep overpotential in the bare Li cell is attributed to the increased electrolyte viscosity caused by extensive electrolyte loss.[52,53] Among the PLs, PL-1 exhibited the most pronounced overpotential increase, while PL-2 and PL-3 showed fewer changes in overpotential. Despite inadequate LiPS blocking, PL-3 self-recovered from the overpotential, achieving a higher Q_L capacity. This, in turn, suggests that the difference in cycling performance under lean electrolyte conditions cannot be fully explained by the efficacy of PLs in inhibiting LiPS permeation or loss. Instead, therefore, the extended cycling of Li–S cells with PL-3 may be attributed to its ability to reduce electrolyte decomposition.

Given that thickness change (swelling) of LMA occurs due to excessive Li pulverization and SEI accumulation during repeated Li cycling, the cross-section SEM images were taken for the LMAs cycled with lean electrolyte. Bare LMA (original thickness: 40 μm) suffered from significant swelling up to 187% (**Figure 3a**), likely

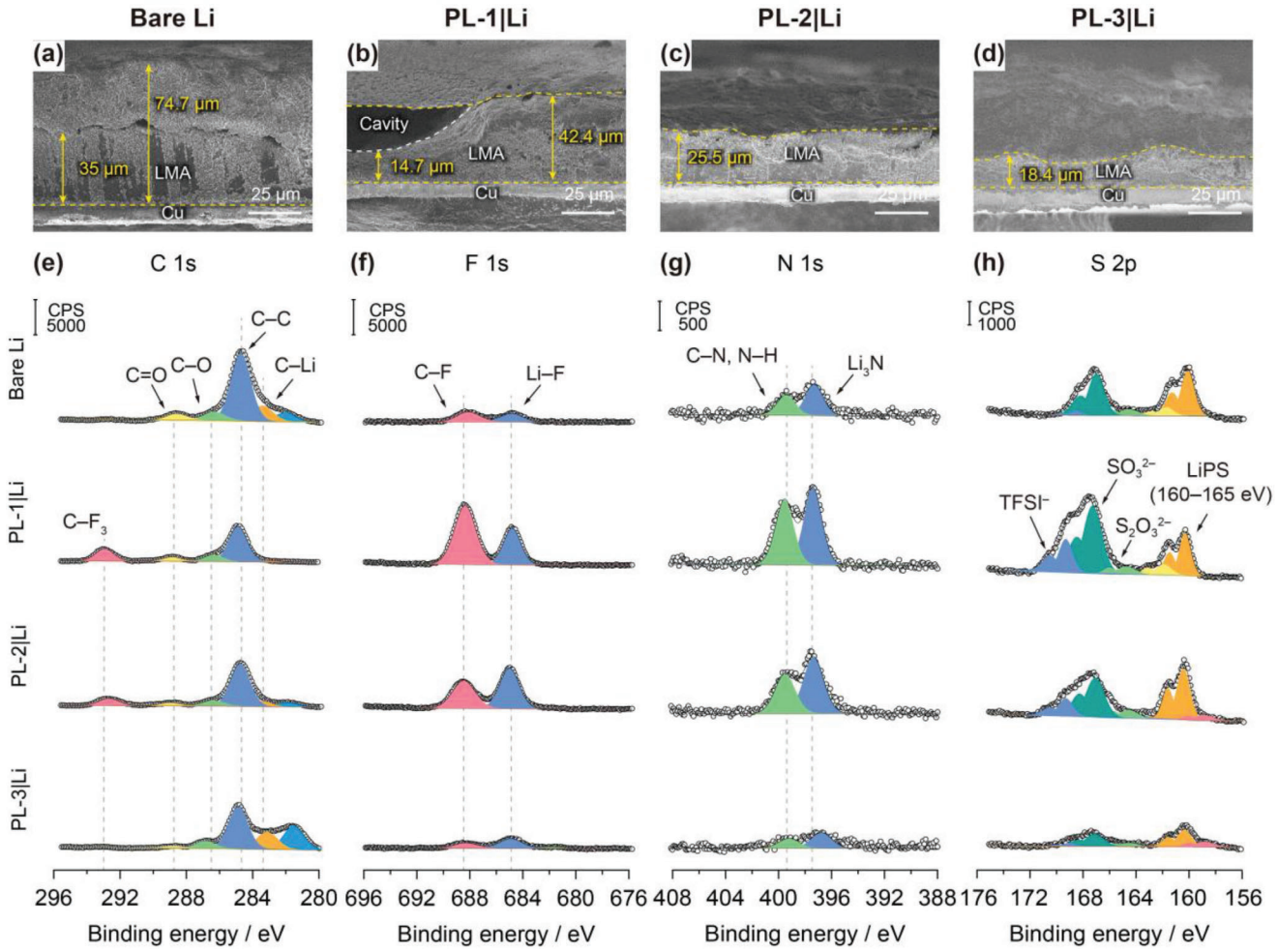

Figure 3. Cross-sectional SEM images for the LMAs obtained from the Li–S cells using a) bare Li, b) PL-1, c) PL-2, and d) PL-3 after 30 cycles under lean electrolyte conditions (E/S = 5 μL mg^{-1}). High-resolution XPS spectra of different elements e) C 1s, f) F 1s, g) N 1s, and h) S 2p at bare Li, PL-1, PL-2, and PL-3. All samples are obtained from LMAs in Li–S full cells after 10 cycles under lean electrolyte conditions (E/S = 5 μL mg^{-1}).

owing to extensive growth of reacted Li layer and non-uniform Li utilization (Figure S5, Supporting Information). The structural evolutions of protected LMAs were distinct. After 30 cycles, the PL-1 exhibited a substantial swelling (106%), and Li pitting-driven huge cavities and local PL delamination were observed (Figure 3b). Thus, the electrolyte could be trapped in-between LMA and PL, intensifying side reactions. However, the PL-2 maintained the physical contact beneath LMA and effectively inhibited electrolyte permeation, resulting in a lower anode swelling of 64% (Figure 3c). Nonetheless, the top view of SEM image after 100 cycles (Figure S6, Supporting Information) confirmed large Li aggregates at the local spots, implying that Li penetration occurred. The PL-3 seemed to have an advantage in suppressing anode swelling, indicating stable structural stability of the PL|LMA interface (Figure 3d). Further insights into similar trends were obtained through an EIS study (Figure S7, Supporting Information). Given that bulk (R_b) and interfacial (R_{int}) resistances serve as indicators of electrolyte decomposition and LMA swelling, respectively, an observed increase in both R_b and R_{int} in the bare Li cell after 100 cycles indicates significant electrolyte decomposition and LMA swelling. Compared to bare Li and other PLs, the PL-1 cell showed significantly higher R_b and R_{int} values after 100 cycles. This suggests that early deterioration of the PL can lead to rapid degradation of the LMA through excessive Li pulverization and subsequent LMA swelling after prolonged cycling. In contrast, R_b values for PL-2 and PL-3 cells stayed relatively stable over 100 cycles, indicating a mitigation of electrolyte decomposition. However, PL-2 cell still exhibited an increase in R_{int} after 100 cycles, whereas PL-3 cell remained consistent even after 100 cycles. Consequently, the extent of LMA swelling after 100 cycles was observed in the following order: PL-1|Li > PL-2|Li ≈ bare Li > PL-3|Li. In this regard, differences in the degradation of the PLs can impact the structural changes of LMAs, emphasizing the importance of ensuring structural stability in the PL|LMA interface.

When performing XPS analysis after peeling off the PLs, notable spectral changes indicate that the extent of side reactions can be varied by the structural stability of PLs (Figure 3e–h). For the PL-1 and PL-2, the F 1s, N 1s, and S 2p peak intensities were more pronounced to the low intensity of the C 1s peak,

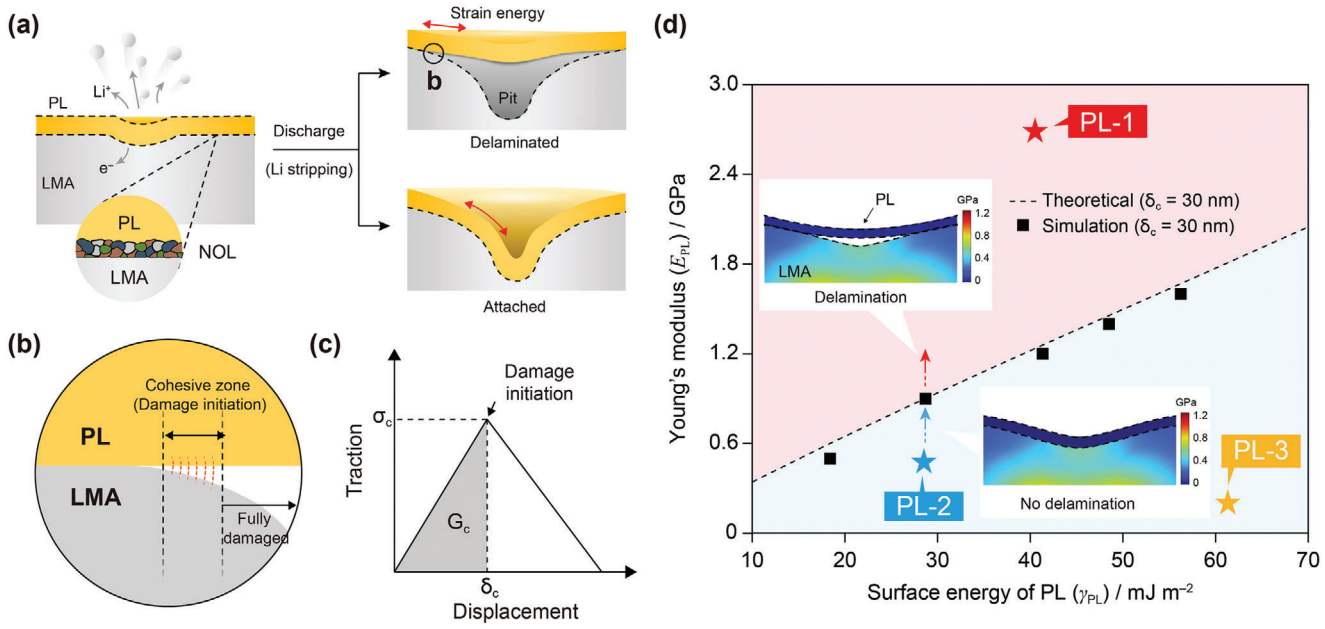

Figure 4. a) Schemes for PL delamination scenario during Li pitting. b) Scheme of cohesive zone model when damage initiation occurs between LMA and PL. c) Traction-separation law (TSL) to deduce the PL delamination threshold, fracture toughness (G_c), which is determined by critical stress (σ_c) and critical displacement (δ_c). The PL|LMA damage is initiated when Γ_0 exceeds beyond G_c. The δ_c was assumed at 30 nm, representing the imaginary gap distance of the adhesion failure limit. d) Surface free energy (SFE)-modulus (γ_{PL}-E_{PL}) plot with theoretical boundary for assessing the PL delamination of three PL models. The onset points of PL|LMA damage (black squares) were extracted from the Solid Mechanic-based COMSOL simulation by iteration of Young's modulus values at the specific SFEs.

implying that the LiTFSI salt decomposition has mainly occurred. Notably, the peaks for C—F, N—H, LiF, and Li_3N, and the S 2p peaks at high binding energy region (sulfate, sulfite, and thiosulfate) were further intensified at the PL-1|LMA interface, implying a severe electrolyte decomposition, likely due to early delamination of PL-1. Thus, improper protection could adversely deteriorate the PL|LMA interface, exacerbating the side reactions with electrolyte trapped in between PL and LMA. While the salt decomposition at the PL-2|LMA interface was less than PL-1|LMA, the PL-2 can partially allow the electrolyte invasion and locally enhance the side reactions compared to bare Li. After prolonged cycles, PL-2 reduced side reactions with LiPS intermediates to some extent. Indeed, thiosulfate ($S_2O_3^{2-}$) peak intensity in the S 2p spectra, which is product of a disproportionation reaction between sulfite and LiPS,[54] was similar to bare Li, whereas overall peak intensities increased (Figure S8, Supporting Information). In contrast, the PL-3 can properly mitigate the decomposition of salt and LiPS than bare Li despite the partial dissolution in the electrolyte, indicating that the PL-3 can alleviate the surface reactivity of LMA. Therefore, ensuring the interfacial stability between LMA and PL is imperative before evaluating electrolyte and LiPS blocking. Despite the beneficial role of LiPS in forming a stable SEI on the LMAs and preventing the growth of Li dendrites,[55] it should be noted that the cycling performance of Li–S cells with lean electrolytes is mostly determined by how the electrolyte loss can be alleviated rather than by the extent of LiPS shuttle suppression. Although polymeric PLs cannot completely prevent LiPS shuttle penetration, the impact of such penetration through PL on cell performance seems negligible, particularly under lean electrolyte conditions. Rather, the modes of PL degradation could play a pivotal role in determining cycle performance. Therefore, it is worth examining the mechanical characteristics of each PL to investigate the root causes behind the variations in PL degradation.

Given that Li–S cell cycling should be initiated by discharge process (Li dissolution occurs), it is worth noting that thin LMA suffers from local pit formation once Li stripping, resulting in the creation of huge cavities (Figure S9a, Supporting Information). Indeed, severe Li pitting exposes beneath Cu surface (Figure S9b, Supporting Information). Such irregular Li dissolution triggers the structural evolution of PL|LMA interfaces, causing a large mechanical stress at the PLs. From this standpoint, we suspect that mechanical failures, especially like delamination, can be mostly initiated by local Li pitting and could cause the deterioration of their protective roles during prolonged cycling. In a mechanical aspect, we hypothesize that PL degradation involves a competitive relationship between the adhesion and stretchability of the PL|LMA interface (**Figure 4a**). Once pit formation is initiated, strain energy (G_S) at the PL increases. To release the stored energy, the PL is going to restore its strain via elastic recovery and compromise the interfacial energy (G_A). Since pit formation was hardly controlled by the PL coating, the mechanical stress induced by Li pitting was consistently applied across all PLs. When subjected to the same tensile deformation stress, a higher Young's modulus corresponds to lower stretchability, indicating a higher tolerance for deformation. If the PL and LMA adhesion is sufficiently high, the PL could endure the deformation and adapt to the created pit. However, when the adhesion and stretchability of PL are poor, it is greater to return to its original state, vulnerable to delamination.

To prove our hypothesis, we first estimate the G_A values by calculating the interfacial energy (Γ) of PL|LMA using the governing Equation 1:

$$\Gamma = \gamma_{Li} + \gamma_{PL} - 2\varphi\left(\gamma_{Li}\gamma_{PL}\right)^{1/2} \quad (1)$$

where γ_{Li} and γ_{PL} are the surface free energies (SFEs) of Li and PL, respectively, and φ is the interaction parameter, assumed as the unity.[56] Here, we did not use the reported γ_{Li} value (398 mJ m^{-2} for pure Li) due to the presence of native oxide layer (NOL).[57,58] Instead, we re-derived the γ_{Li} (≈196 mJ m^{-2}) by confirming the actual NOL compositions via the XPS spectra (Figure S10, Supporting Information) and referring to SFE data of each component (Table S1, Supporting Information). Through Owens–Wendt method,[59] we collected the γ_{PL} values for each PL (Figure S11, Supporting Information) and corresponding Γ values were depicted in Figure S12 (Supporting Information). Through the strain-stress curves, we determined Young's modulus (E_{PL}) (Figure S13, Supporting Information). According to fracture mechanics,[60] work of fracture (Γ_0), the driving force per unit length of the separation line during delamination, can be represented as the delamination threshold and can be described as below Equation 2:

$$\Gamma_0 = \gamma_{Li} + \gamma_{PL} - \Gamma \quad (2)$$

$$\Gamma_0 \propto \gamma_{PL}{}^{1/2} \quad (3)$$

Combining Equations 1 and 2, it was found that Γ_0 values can be defined by the γ_{PL} values (Equation 3). The calculated Γ_0 values are situated within a reasonable range for the interaction between LMA and PLs, consistent with findings in previous studies.[61,62] To link the mechanical strength of PLs with SFE-determined Γ_0, a cohesive zone approach was exploited (Figure 4b). Considering the initial deformation of both PL and LMA within the elastic range, a bilinear traction-separation law can be employed (Figure 4c). To simplify the model, we assumed that tensile and shear damage modes were identically contributed. PL delamination is initiated when Γ_0 exceeds beyond the fracture toughness (G_c), which can be governed by Equation 4 and determined by critical stress (σ_c) or critical displacement (δ_c). The δ_c can be assumed at constant (30 nm), which indicates the imaginary gap distance of the adhesion failure point.

$$G_c = \frac{1}{2}\sigma_c\delta_c \quad (4)$$

$$\sigma_c^* = \frac{2\Gamma_0}{\delta_c} = \frac{4\varphi\left(\gamma_{Li}\gamma_{PL}\right)^{\frac{1}{2}}}{\delta_c} \quad (5)$$

Integrating the derived relationship between G_c and SFE-determined Γ_0, Equation 5 can be derived. The maximum traction (critical stress) can be decreased as the SFE of PL decreases. Therefore, E_{PL} should be mildly tuned considering the SFE-determined Γ_0 to secure the surface adaptivity of PLs. In other words, despite less adhesive (low γ_{PL}), the PL delamination could be staved off by reducing the E_{PL}.

In this regard, we preliminary presented the SFE-modulus (γ_{PL}-E_{PL}) plot using COMSOL simulation (Figure 4d). More details including the models (Figures S14 and S15, Supporting Information), and parameters (Table S2, Supporting Information), are described in the Supporting Information. First, it was verified that an increase in E_{PL} and PL thickness can easily trigger the delamination (Figure S16, Supporting Information). From the previous studies,[63,64] Young's modulus and the coating layer thickness are identified as the key material parameters affecting delamination in bilayer systems. When the PL thickness and δ_c were set to 3 μm and 30 nm, respectively, the γ_{PL}-E_{PL} plot reveals that PL-2 could maintain the contact despite its lower γ_{PL}, since the E_{PL} is lower than the critical value. Although the γ_{PL} of PL-1 is higher than that of PL-2, E_{PL} of PL-1 exceeds critical modulus, leading to immediate delamination and failure to adapt to local Li pitting. While this finding may contradict the consensus regarding PL requirements, where a high modulus is preferred for mechanically suppressing Li dendrites,[65,66] our simulation study provides insight into how to ensure the structural stability of the PLs against Li pitting-induced delamination. Particularly for deformation-tolerable, high-modulus PLs, the adhesion (γ_{PL}) must be significantly increased to prevent PL delamination. Therefore, increasing γ_{PL} should be co-considered for high modulus PL to secure the interface stability of PL|LMA, indicating the potential importance of these factors in material selection.

To examine the morphological evolution of PL|LMA, we performed an ex situ SEM study for the LMA samples harvested after the first discharge (first Li stripping), recharge (subsequent Li plating), and second discharge (Li re-stripping) steps. The bare Li suffered from severe local Li pitting, even exposing beneath Cu (**Figure 5a–d**), and dendritic Li was deposited locally at the pit area during subsequent charging. Then, Li can be stripped out at the Li dendrites and unstripped Li area, resulting in irregular surface morphology even after pre-cycling. While local Li pitting was consistently observed despite PL coating, degradation patterns were different. The PL-1 looks instantly delaminated upon first Li stripping. The contrast difference during the following recharge and discharge indicates the silhouettes juxtaposed with the roughened LMA surface beneath the PL-1. In contrast, PL-2 maintained interfacial contact along the pitted surfaces, implying that a highly elastic nature with lower E_{PL} compensates the insufficient adhesion. Nonetheless, Li penetration took place eventually where PL-2 could not withstand the Li dendrite-driven deformation, leading to gradual deterioration of the interfacial contact. The PL-3 can also adapt to the Li pitting benefiting from the lowest interfacial energy, while its partial dissolution adversely causing Li deposition and propagation along atop the PL.

Figure 5e illustrates the PL degradation behaviors regarding the structural stability of PL|LMA interfaces. Despite the Li protection, sporadic Li pitting could be occurred owing to inherently inhomogeneous NOL or irregularity of bulk Li structure.[67,68] Once the Li pitting severely occurred, PL deformation is inevitable. While good adhesion is beneficial, if the PL is not sufficiently deformable, delamination could occur (PL-1). The failure of Li protection with earlier delamination causes the invasion of electrolyte and LiPS into the interspace between PL and LMA, accelerating the LMA deterioration. Despite the relatively weaker adhesion to LMA, the highly deformable PL could adapt to the Li pitting-driven interfacial evolution, effectively retard the delamination (PL-2). Nonetheless, the low modulus of PL could be fatal to Li penetration, eventually leading to partial

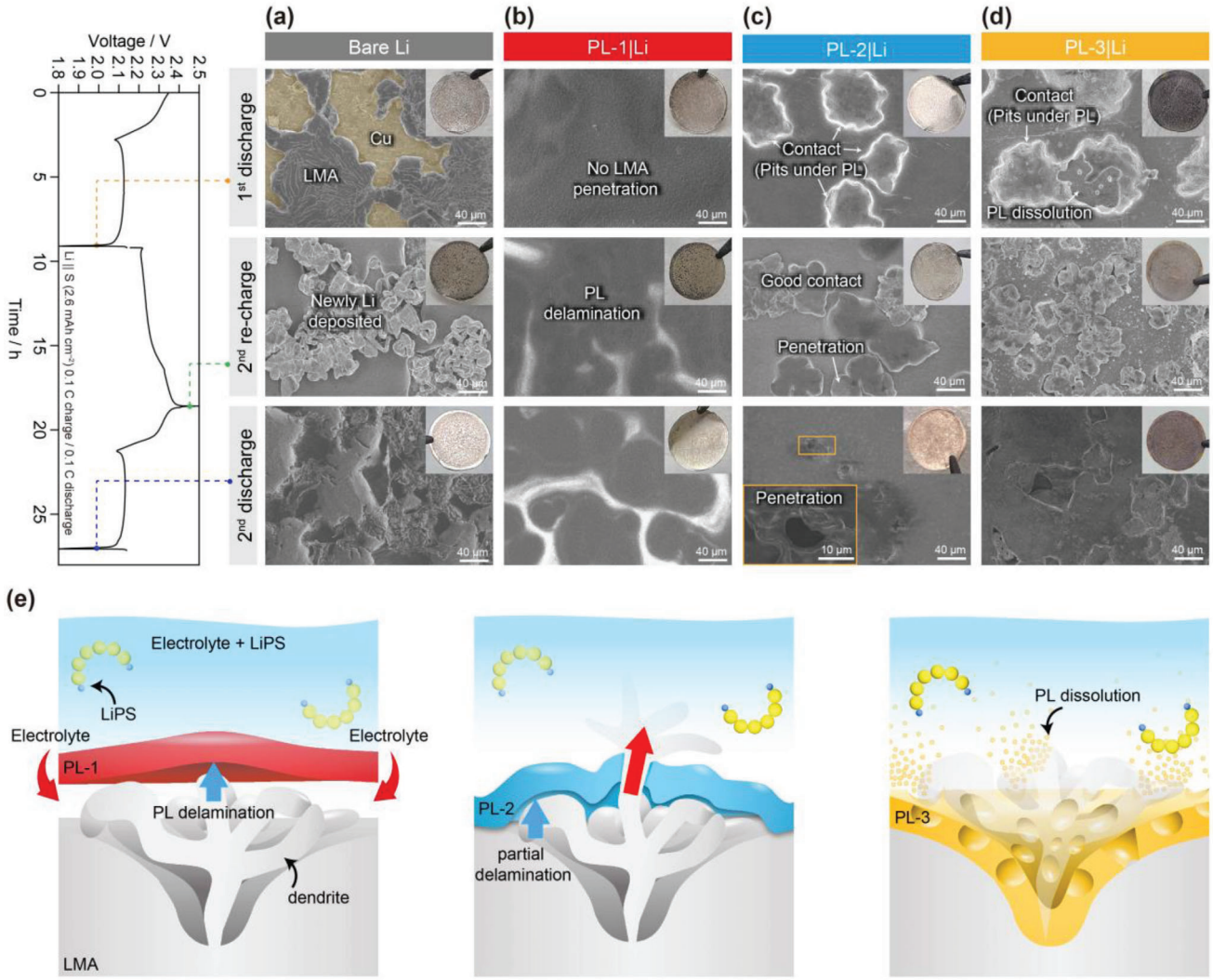

Figure 5. Ex situ SEM analysis for the LMA samples harvested after the first discharge (first Li stripping), recharge (followed Li plating), and second discharge (second Li stripping) steps, as depicted in the voltage curve of Li–S cell (2.6 mAh cm^{-2}) cycled at 0.1 C-rate: a) bare Li; b) PL-1; c) PL-2; and d) PL-3. e) Schemes of PL degradation, including PL delamination, Li penetration, and PL dissolution, respectively.

delamination. The PL possessing a higher γ_{PL} is preferred to prevent the Li pitting-driven delamination (PL-3). Although the proposed SFE-modulus (γ_{PL}-E_{PL}) map should be refined through precise adjustments of key variables in the simulation and further validated with various PL candidates, the γ_{PL} and E_{PL} values of the PL can serve as indicators to identify suitable PL candidates for effective LMA protection.

The above mechanistic studies have inspired us to design a dual-layer structured PL focusing on interfacial energy and elasticity to enhance surface adaptivity for sustainable protection. The dual-layered APL includes the PL-3 (PEO) inner layer for reducing PL|LMA interfacial energy, positioning well-stretchable PL-2 (PVDF-HFP) at the outmost layer for LiPS rejection (**Figure 6**a). In a mechanical aspect, the Young's modulus of APL was measured at 0.58 GPa using UTM (Figure S17, Supporting Information), which is not positioned at the midpoint between PL-3 (0.26 GPa) and PL-2 (0.54 GPa), but it is consistent with that of PL-2. This suggests that the mechanical strength of dual-layered APL is governed by its more robust component. Benefiting from PL-2, the APL effectively mitigated the LiPS crossover in the H-cell test (Figure S18, Supporting Information). Furthermore, the outer coating of PL-2 is essential to prevent the partial dissolution of PL-3 (PEO) into the electrolyte. Cross-section SEM image reveals that APL was successfully coated and distinct composition (C, F, and O) by tracking the EDS mapping (Figure 6b). Ex situ SEM study was further conducted to examine the surface adaptivity of APL during initial cycling at 0.1 C rate. In contrast to extreme structural change of bare Li, the structure of APL well-remained without delamination upon first Li stripping (Figure 6c), benefiting from the PEO inner layer, and showed no penetration subsequent Li plating (Figure 6d), ensuring high stretchability. Even after 2nd discharge, no delamination and penetration were observed (Figure 6e), emphasizing that improving surface adaptivity by reducing interfacial energy and ensuring stretchable characteristic is key role for suppressing the initial degradation. Moreover,

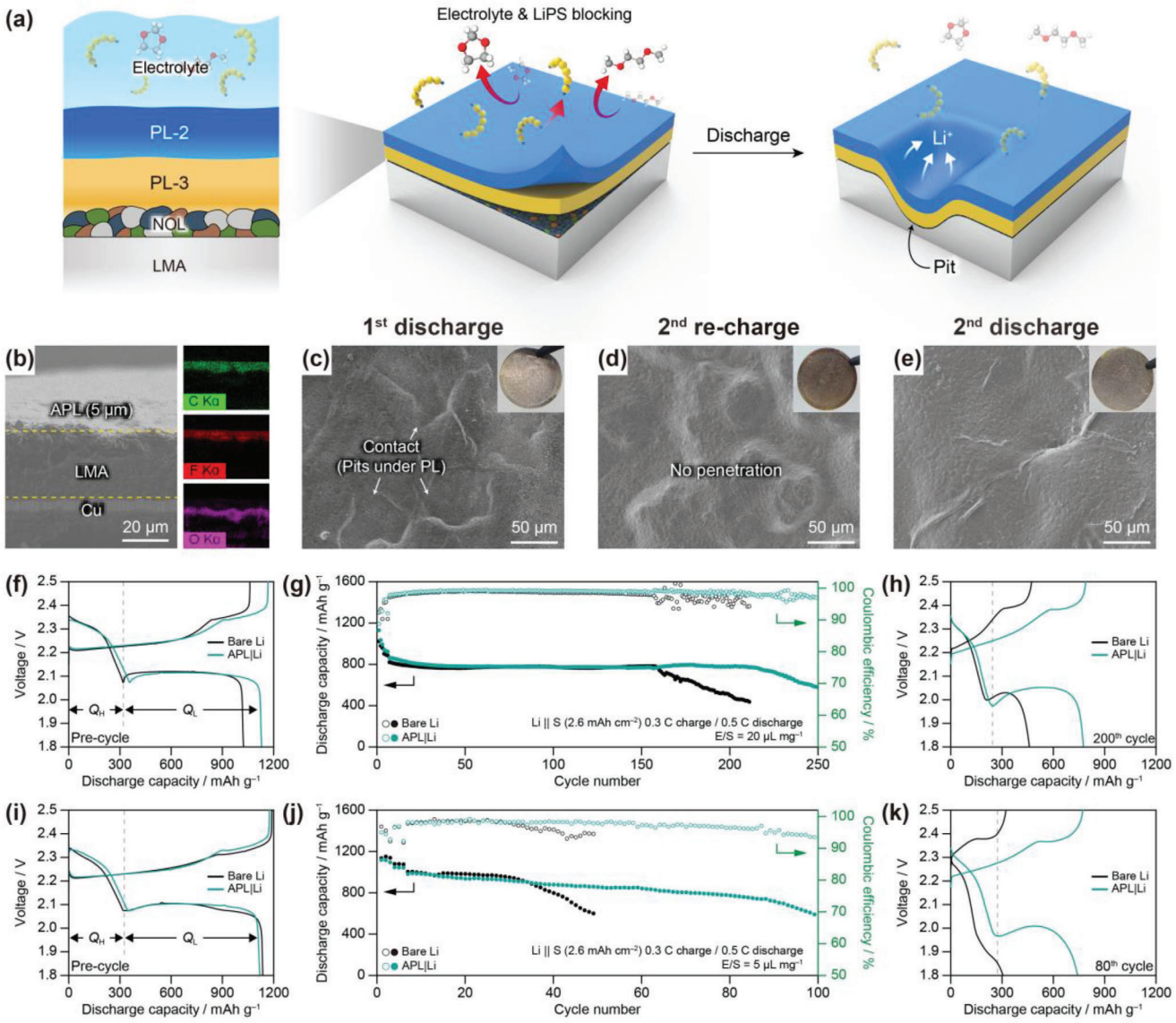

Figure 6. Design and morphological evolution of APL-coated LMA and cycling performance of Li–S cells. a) Scheme of APL structure. b) Cross-sectional SEM image with EDS mapping of APL. Ex situ SEM images obtained after c) discharge, d) re-charge, and e) second discharge at 0.1 C. f) Pre-cycling voltage profiles, g) capacity retentions, and h) post-cycling voltage profiles (after 200 cycles) for Li–S cells with bare Li and APL|Li cycled under flood electrolyte (E/S = 20 μL mg^{-1}) at 0.3 C/0.5 C charge/discharge. i) Pre-cycling voltage profiles, j) capacity retentions, and k) post-cycling voltage profiles (after 80 cycles) for Li–S cells with bare Li and APL|Li cycled under lean electrolyte (E/S = 5 μL mg^{-1}) at 0.3 C/0.5 C charge/discharge.

postmortem SEM revealed that the APL remained intact and preserved its original morphology despite repeated cycling (Figure S1, Supporting Information9). EDS mapping also confirmed that the oxygen component, attributed to the PEO layer, remained located at the bottom of the APL, implying the suppression of PEO dissolution.

To validate the impact of APL, the cycling stability of Li–S cells under flooded- and lean-electrolyte conditions was evaluated. When cycling with flooded electrolyte (Figure 6f), the cell with APL|Li attained a higher capacity (1130 mAh g^{-1}) and delivered longer cycle-life (224 cycles) at 80% capacity retention, superior to unprotected LMA (168 cycles) (Figure 6g). While Q_H was consistently reduced in both cells after 200 cycles, the APL|Li cell retained much higher Q_L, suggesting that APL effectively suppressed permeation of LiPS (Figure 6h). Because APL|Li maintained adhesion well, it physically blocked LiPS, thereby retarding the reaction between LiPS and LMA. Moreover, the APL|Li cells with mildly low E/S ratio (8.5 μL mg^{-1}) consistently improved the cycle performance (193→286 cycles) (Figure S20, Supporting Information). When further reducing the E/S ratio (5 μL mg^{-1}), the protective role of APL becomes more pronounced, simultaneously enhancing Q_H and Q_L retentions with reduced cell polarization (Figure 6i,k), which are unattainable for bare Li. This improvement is likely attributed to suppression of electrolyte consumption, demonstrating a twofold enhancement of cycling performance (38→87 cycles at 70% capacity retention) (Figure 6j).

In the cyclic voltammetry (CV) test (Figure S21, Supporting Information), the cathodic peak at 1.9–2.0 V, attributed to LiPS reduction, was significantly delayed for the bare Li cell during repeated CV cycles. This delay indicates that the LiPS reduction kinetics become sluggish, likely due to an increase in viscosity driven by electrolyte loss.[69] However, the APL|Li cell exhibited a negligible peak shift, suggesting that APL protection can alleviate electrolyte decomposition without significantly increasing viscosity, thus ensuring seamless electrochemical reduction.

For a comparison with other single-layer PLs, we fairly equalized the thickness of PLs and APL at 5 μm and performed the Li–S cell cycling test under lean electrolyte conditions (Figure S22, Supporting Information). Indeed, similar trends were observed for single-layer PLs: the PL-2 and −3 cells showed extended cycle numbers, while PL-1 cell failed earlier, showing sudden capacity drop after only 18 cycles. This implies that the increased thickness of the high modulus PL (PL-1) not only makes it more susceptible to delamination but also accelerates side reactions of electrolytes trapped between the PL and LMA, which is well supported by our simulation results (Figure S16, Supporting Information). In stark contrast, 5 μm-APL demonstrates outstanding cycling stability among the PLs and remains superior to thinner single-layer PLs (3 μm), as shown in Figure 2. Despite the thickness penalty, the extended cycling performance of the APL cell under lean electrolyte conditions can be firmly attributed to its surface adaptive function, which plays a crucial role amidst the structural evolution of the underlying LMA. Indeed, when the thickness of the APL is doubled to ≈10 μm, its surface adaptive function may be limited in preventing electrolyte decomposition, as confirmed by Li–S cell cycling results (Figure S23, Supporting Information).

To further validate the surface adaptivity role of APL, we conducted additional experiments with a reversed APL (rAPL) by changing the coating sequence of PL-2 and PL-3 and performed the cycling test with Li–S full cells using bare Li, APL|Li, and rAPL|Li under lean electrolyte condition (Figure S24, Supporting Information). The cell with rAPL|Li showed inferior cycle performance compared to bare Li and APL|Li cells (<40 cycles with 80% capacity retention). When exposing the PL-3 to the electrolyte, it can be dissolved into the electrolyte as confirmed before (Figure S4, Supporting Information), leading to a sole protection with inner layer (PL-2, PVDF-HFP), not securing the interfacial stability, and thereby leading to imperfect surface adaptivity. Moreover, using PEO as the outer layer is not preferred, as it adversely permits the penetration of sulfur or LiPS.[70] Benefiting from the rational sequencing of dual-layer coating, the APL can inhibit the electrolyte penetration by PEO-derived improvement of the PL|LMA interfacial stability and prevent LiPS crossover through the outer PVDF-HFP. The efficacy of APL was further verified by performing the rate capability test of Li–S cells (Figure S25, Supporting Information).[71,72] Contrary to bare Li, the APL cell retained the higher cell capacity even at escalated discharge rates by alleviating the overpotential of the 2nd voltage plateau, likely attributed to the lower viscosity of the electrolyte.

To compare the extent of Li pulverization, the cross-sectional SEM images of the bare Li and APL|Li were collected under different electrolyte conditions. With 8.5 μL mg^{-1} of E/S ratio, unprotected Li underwent 162% of anode swelling, whereas APL-Li exhibited only 70% of anode swelling after 150 cycles (**Figure 7**a,b). Similar behaviors were consistently observed at different local spots (Figure S26, Supporting Information). Even at a lower E/S ratio (5 μL mg^{-1}), while bare Li severely suffered from LMA swelling (187%, Figure 7c), APL exhibited only 70% of LMA swelling (Figure 7d), suggesting that APL could retard the Li pulverization and minimize side reactions by improved surface adaptivity against the structural evolution of PL|LMA interfaces. To further evaluate the protective role, we examined the XPS spectra evolutions for bare Li and APL|Li after 10 cycles under lean electrolyte (Figure 7e–h). Bare Li showed remarkable peaks of N and S-containing species, including C—N, N—H (399.3 eV) and Li_3N (397.3 eV) in N 1s spectra and $-SO_x$ (167 eV), $-S_2O_x$ (168 eV), and LiPS derivatives (LiS_2, Li_2S_2 and S—S species) at lower binding energies (160–165 eV) in the S 2p spectra. In contrast, APL|Li exhibited much weaker S-containing peaks, suggesting that effective prevention of LiTFSI and LiPS-derived side reactions. When examining the top-view SEM images after 25 cycles, bare Li showed a dendritic and mossy Li deposits, whereas APL exhibits a comparatively smoother structure (Figure S27, Supporting Information). This contrast is responsible to surface adaptability of APL accommodating LMA swelling-driven structural evolution and sustaining interfacial contact. Therefore, reinforcing the PL|LMA interfacial stability using dual-layer structured APL can successfully inhibit the penetration of electrolyte and LiPS, which is crucial for LMA stabilization in the practical Li–S cells.

3. Conclusion

In this work, we proposed the APL concept to protect LMA sustainably and to secure the cycling performances of Li–S batteries with lean electrolytes. Despite the conformal coating of PL, the intrinsic heterogeneity of the LMA surface can still induce uneven Li stripping and plating. Our experimental results and simulation study on the PL failure mechanism emphasize the significance of two properties of PLs: interfacial stability (adhesion) and stretchability. In lean electrolyte conditions, the cycling stability of Li–S cells with PL-coated LMAs relies on how well the PL can alleviate electrolyte depletion and maintain the PL|LMA interface during uncontrolled structural evolution of the LMAs. Dual-layered APL can simultaneously improve the PL|LMA interface stability via PEO inner layer and the LiPS blocking by outer coating of elastic PVDF-HFP, demonstrating surface-adaptive protection of LMA. The Li–S cells with the APL|LMA successfully validates the extended cycling even at low E/S ratio by alleviating the Li pulverization and electrolyte loss. The proposed SFE-modulus plot should be developed by finely tuning the key variables and further validation with various PL candidates. If the extent of electrolyte loss is closely related to the initial PL failure, Young's modulus and SFE values for the PL of interest could be strong indicators for ensuring the structural stability of PL|LMA interfaces and determining the cyclability of practical Li–S cells.

4. Experimental Section

Fabrication of PL-Li: All procedures were in Ar-filled glove box (moisture and oxygen content ≤ 0.1 ppm). 10 wt.% polymer (PVDF, PVDF-HFP) solutions were dissolved in Dimethylacetamide (DMAc, Sigma–Aldrich)

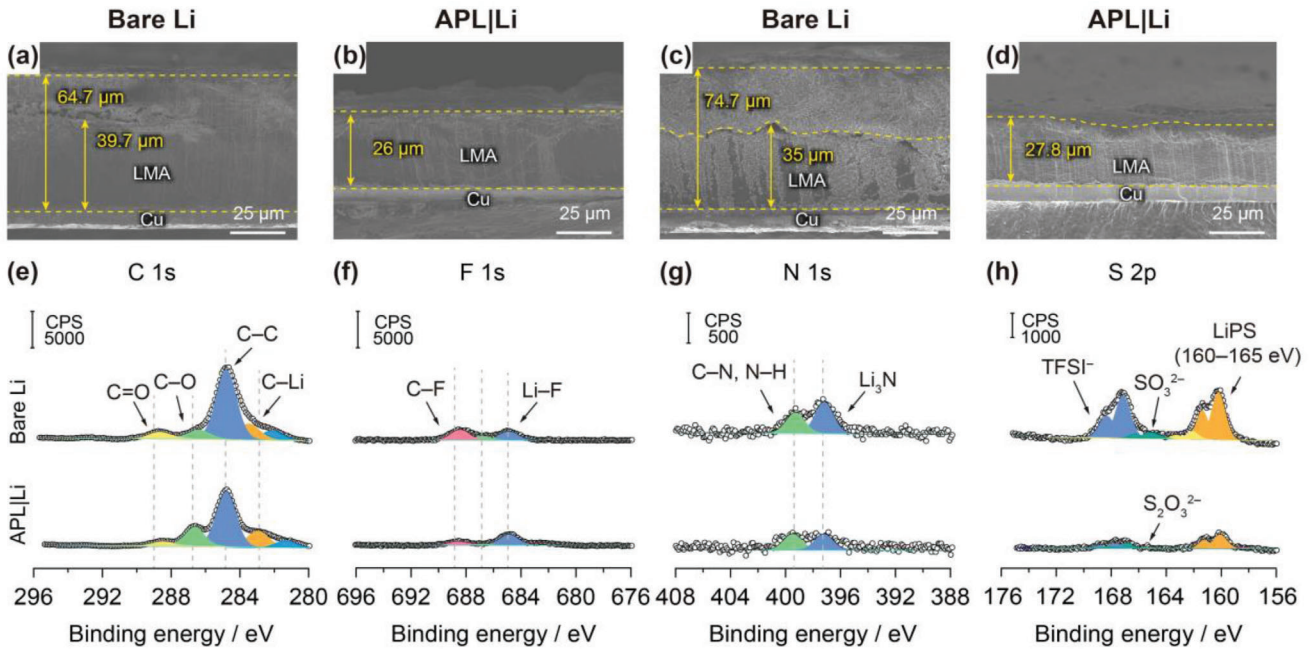

Figure 7. Postmortem analysis of bare Li and APL. Swelling test of LMAs obtained from Li–S cell after 150 cycles under electrolyte condition (E/S ratio 8.5 μL mg^{-1}) using a) bare Li, b) APL. Swelling test of LMAs obtained from Li–S cell after 30 cycles under electrolyte condition (E/S ratio 5 μL mg^{-1}) using c) bare Li, d) APL. High-resolution XPS spectra of different elements (e) C 1s, f) F 1s, g) N 1s, and h) S 2p) at the Bare Li and APL, respectively. All samples are obtained from LMAs in Li–S cell after 10 cycles at E/S ratio 5 μL mg^{-1}.

and mechanically stirred to make a homogeneous solution. 10 wt.% of PEO (Mw 100 000, Sigma–Aldrich) was put in DMAc and mechanically stirred at 60 °C until PEO was entirely dissolved. The solution was cast on the Li foil (40 μm thick Li laminate, Honjo Co.Ltd, Japan) using a doctor blade and dried to evaporate DMAc solvents at 60 °C under a chamber in the glove box for 1 h. For taking APL, PVDF-HFP solution cast the PEO-coated LMA to coat the OPL.

Material Characterization: To study the morphological feature of PLs, field-emission scanning electron microscopy (FE-SEM, SU−8020, S-4800, Hitachi, Japan) was used. Atomic force microscopy (AFM, Nanosurf, Swiss) was used to investigate 2D and 3D surface topology and quantify the roughness of bare Li and PL-Li in non-contact mode. The contact angles were investigated using a DSA100 (USA) using two different solvents (water, ethylene glycol) to estimate the surface free energy of the PLs. All the mechanical properties of PLs were measured by Universal testing machine (UTM, SFM-100 kN, USA). The PL films were casted (≈0.1 mm thickness) onto the glass and then dried at 60 °C under convection oven for overnight. The LiPS diffusion test was conducted in two compartment H-cell with compartments separated by polymer-based PL (120 μm thickness, diameter:20 mm) and PE separator (diameter:19 mm). The left side contained DOL/DME solvent, while the right side contained 0.5 M Li_2S_6 in DOL/DME, aiming to replicate authentic cell conditions. The LiPS solution was prepared by dissolving stoichiometric amounts of Li_2S and S_8 in DOL/DME (1:1 in volume) and stirred at room temperature overnight. The diffusion test was performed in the glove box (H_2O and O_2 content ≤0.1 ppm) for 30 h.

Electrochemical Measurements: All coin-type cells (CR2032) were assembled in a glove box. The cathode was prepared by LG Energy Solution. The areal sulfur loading was fixed at 2.3 mg_{sulfur} cm^{-2}. Coin cells were fabricated in an Ar-filled glove box by pairing with a 40 μm-thick Li laminate on copper current collector (diameter:16 mm, Honjo Co.Ltd, Japan) discs as a counter electrode. A polyethylene membrane (diameter:19 mm, PE, LG Energy Solution) was used as a separator. Electrolytes with LiTFSI and lithium nitrate ($LiNO_3$) were prepared, totaling a Li^+ concentration of 1 M in 1,3-dioxolane (DOL): 1,2-dimethoxyethane (DME) (1:1 in volume) and 2 wt.% $LiNO_3$. The variable E/S ratio was used at 20, 8.5, 5 μL mg^{-1}_{sulfur} for each cell. The Li–S cells with mass-loading of cathode (≈2.6 mAh cm^{-2}) were cycled 2.5 times at 0.1 C rate over the voltage range of 1.8–2.5 V and subsequent cycling was performed at 0.2 C rate three times for formation cycle at 25 °C. And then, main cycling was performed at 0.3 C charge (constant current (CC) mode) and 0.5 C discharge (CC mode) current density within the same voltage window.

Postmortem Analysis: The cycled cells were disassembled inside the glove box. All samples were washed with pure DME solvent and dried at room temperature under a vacuum overnight. Then, the samples were hermetically sealed using polypropylene containers and were quickly transferred to the SEM and XPS chambers to avoid sample contamination. The chemical components of the passivation layer of bare Li and PL|LMA surfaces were examined using XPS (ESCALAB 250Xi, Thermo Fisher Scientific, USA). The Casa XPS program was used for peak deconvolution. The C 1s peak at 284.8 eV was taken as a reference to calibrate the binding energy of all elements. To obtain 3D topology after the pit formation, Li–S cells were discharged at 0.1 C rate and the cell was disassembled after 0.1 mAh cm^{-1}.

Computational Simulation: To comprehend the properties of the PL and its impact on delamination, a delamination model of the PL|LMA was developed using Solid Mechanics module in COMSOL Multiphysics 6.0. From the literature,[73] the geometric and mechanical parameters were derived from experiments and assumptions (Table S2, Supporting Information). Geometric features, boundary conditions, and initial conditions are detailed in Figure S14 (Supporting Information). To simulate the pit formation as Li stripped out, a hygroscopic shrinkage region was created within the LMA. This induced strong interfacial stress between the PL and LMA due to Li-induced strain. Work of fracture (Γ_0) values were calculated from the SFEs of each material to implement the adhesive behavior of the interface, and the relationship between SFEs and critical stress was also derived through the introduction of bilinear traction-separation law. Interfacial energy (Γ) was diagnosed by evaluating the onset of damage according to the SFEs (γ_{PL}) and Young's modulus (E_{PL}) of the PL materials using derived a relationship.

Supporting Information

Supporting Information is available from the Wiley Online Library or from the author.

Acknowledgements

B.C., K.G.K., and M.L. contributed equally to this work. This research was supported by the Technology Innovation Program (No. 20015759) funded by the Korean Ministry of Trade, Industry, and Energy (MOTIE) and the National Research Foundation (NRF) of Korea (RS-2023-00222166). The authors extend their special thanks for insightful discussions and funding support from LG Energy Solution. H.Lee especially thanks to the support from the Brain Korea 21 FOUR Project at DGIST.

Conflict of Interest

The authors declare no conflict of interest.

Data Availability Statement

The data that support the findings of this study are available from the corresponding author upon reasonable request.

Keywords

dual-layer protection, lean electrolytes, lithium-metal anodes, lithium–sulfur batteries, surface-adaptive protection

Received: December 30, 2023
Revised: February 25, 2024
Published online: March 12, 2024

[1] X.-B. Cheng, R. Zhang, C.-Z. Zhao, Q. Zhang, *Chem. Rev.* **2017**, *117*, 10403.
[2] W. Xu, J. Wang, F. Ding, X. Chen, E. Nasybulin, Y. Zhang, J.-G. Zhang, *Energy Environ. Sci.* **2014**, *7*, 513.
[3] P. Albertus, S. Babinec, S. Litzelman, A. Newman, *Nat. Energy* **2018**, *3*, 16.
[4] N.-S. Choi, Z. Chen, S. A. Freunberger, X. Ji, Y.-K. Sun, K. Amine, G. Yushin, L. F. Nazar, J. Cho, P. G. Bruce, *Angew. Chem., Int. Ed.* **2012**, *51*, 9994.
[5] X. Ji, K. T. Lee, L. F. Nazar, *Nat. Mater.* **2009**, *8*, 500.
[6] Y. Yang, G. Zheng, Y. Cui, *Chem. Soc. Rev.* **2013**, *42*, 3018.
[7] A. Manthiram, Y. Fu, S.-H. Chung, C. Zu, Y.-S. Su, *Chem. Rev.* **2014**, *114*, 11751.
[8] M. Barghamadi, A. S. Best, A. I. Bhatt, A. F. Hollenkamp, M. Musameh, R. J. Rees, T. Rüther, *Energy Environ. Sci.* **2014**, *7*, 3902.
[9] S. S. Zhang, *Electrochim. Acta* **2012**, *70*, 344.
[10] S. Xiong, K. Xie, Y. Diao, X. Hong, *J. Power Sources* **2014**, *246*, 840.
[11] J. He, A. Manthiram, *Energy Storage Mater.* **2019**, *20*, 55.
[12] L. F. Nazar, M. Cuisinier, Q. Pang, *MRS Bull.* **2014**, *39*, 436.
[13] H. Kwon, J. Baek, H.-T. Kim, *Energy Storage Mater.* **2023**, *55*, 708.
[14] G. Zhou, H. Chen, Y. Cui, *Nat. Energy* **2022**, *7*, 312.
[15] S.-H. Chung, C.-H. Chang, A. Manthiram, *Adv. Funct. Mater.* **2018**, *28*, 1801188.
[16] Y.-T. Liu, S. Liu, G.-R. Li, X.-P. Gao, *Adv. Mater.* **2021**, *33*, 2003955.
[17] H. Pan, K. S. Han, M. H. Engelhard, R. Cao, J. Chen, J.-G. Zhang, K. T. Mueller, Y. Shao, J. Liu, *Adv. Funct. Mater.* **2018**, *28*, 1707234.
[18] S.-H. Kang, X. Zhao, J. Manuel, H.-J. Ahn, K.-W. Kim, K.-K. Cho, J.-H. Ahn, *Phys. Status Solidi (a)* **2014**, *211*, 1895.
[19] M. Zhao, B.-Q. Li, X.-Q. Zhang, J.-Q. Huang, Q. Zhang, *ACS Cent. Sci.* **2020**, *6*, 1095.
[20] C. Barchasz, J.-C. Leprêtre, F. Alloin, S. Patoux, *J. Power Sources* **2012**, *199*, 322.
[21] M. Zhao, B.-Q. Li, H.-J. Peng, H. Yuan, J.-Y. Wei, J.-Q. Huang, *Angew. Chem., Int. Ed.* **2020**, *59*, 12636.
[22] Y. V. Mikhaylik, J. R. Akridge, *J. Electrochem. Soc.* **2004**, *151*, A1969.
[23] Q. Jin, X. Qi, F. Yang, R. Jiang, Y. Xie, L. Qie, Y. Huang, *Energy Storage Mater.* **2021**, *38*, 255.
[24] D. Han, X. Wang, Y.-N. Zhou, J. Zhang, Z. Liu, Z. Xiao, J. Zhou, Z. Wang, J. Zheng, Z. Jia, B. Tian, J. Xie, Z. Liu, W. Tang, *Adv. Energy Mater.* **2022**, *12*, 2201190.
[25] S. Zheng, H. Geng, S. N. Eliseeva, B. Wang, *Energy Mater* **2022**, *2*, 200042.
[26] Y. Jo, D. Jin, M. Lim, H. Lee, H. An, J. Seo, G. Kim, X. Ren, Y. M. Lee, H. Lee, *Adv. Sci.* **2023**, *10*, 2204812.
[27] X. Xu, S. Wang, H. Wang, B. Xu, C. Hu, Y. Jin, J. Liu, H. Yan, *J. Energy Storage* **2017**, *13*, 387.
[28] L. Shi, S.-M. Bak, Z. Shadike, C. Wang, C. Niu, P. Northrup, H. Lee, A. Y. Baranovskiy, C. S. Anderson, J. Qin, S. Feng, X. Ren, D. Liu, X.-Q. Yang, F. Gao, D. Lu, J. Xiao, J. Liu, *Energy Environ. Sci.* **2020**, *13*, 3620.
[29] Y. Huang, L. Lin, C. Zhang, L. Liu, Y. Li, Z. Qiao, J. Lin, Q. Wei, L. Wang, Q. Xie, D.-L. Peng, *Adv. Sci.* **2022**, *9*, 2106004.
[30] Y. M. Lee, N.-S. Choi, J. H. Park, J.-K. Park, *J. Power Sources* **2003**, *119–121*, 964.
[31] E. Cha, M. D. Patel, J. Park, J. Hwang, V. Prasad, K. Cho, W. Choi, *Nat. Nanotechnol.* **2018**, *13*, 337.
[32] Q. Jin, X. Zhang, H. Gao, L. Li, Z. Zhang, *J. Mater. Chem. A* **2020**, *8*, 8979.
[33] J. Luo, C.-C. Fang, N.-L. Wu, *Adv. Energy Mater.* **2018**, *8*, 1701482.
[34] Y. Liu, D. Lin, P. Y. Yuen, K. Liu, J. Xie, R. H. Dauskardt, Y. Cui, *Adv. Mater.* **2017**, *29*, 1605531.
[35] Z. Han, C. Zhang, Q. Lin, Y. Zhang, Y. Deng, J. Han, D. Wu, F. Kang, Q.-H. Yang, W. Lv, *Small Methods* **2021**, *5*, 2001035.
[36] X. Yu, S. Feng, M. J. Boyer, M. Lee, R. C. Ferrier, N. A. Lynd, G. S. Hwang, G. Wang, S. Swinnea, A. Manthiram, *Mater. Today Energy* **2018**, *7*, 98.
[37] N. Yan, X. Yang, W. Zhou, H. Zhang, X. Li, H. Zhang, *RSC Adv.* **2015**, *5*, 26273.
[38] M. Li, Y. Wan, J.-K. Huang, A. H. Assen, C.-E. Hsiung, H. Jiang, Y. Han, M. Eddaoudi, Z. Lai, J. Ming, L.-J. Li, *ACS Energy Lett.* **2017**, *2*, 2362.
[39] Z. Wang, W. Huang, J. Hua, Y. Wang, H. Yi, W. Zhao, Q. Zhao, H. Jia, B. Fei, F. Pan, *Small Methods* **2020**, *4*, 2000082.
[40] J.-Q. Huang, Q. Zhang, H.-J. Peng, X.-Y. Liu, W.-Z. Qian, F. Wei, *Energy Environ. Sci.* **2014**, *7*, 347.
[41] T.-Z. Zhuang, J.-Q. Huang, H.-J. Peng, L.-Y. He, X.-B. Cheng, C.-M. Chen, Q. Zhang, *Small* **2016**, *12*, 381.
[42] J. Lee, J. Song, H. Lee, H. Noh, Y.-J. Kim, S. H. Kwon, S. G. Lee, H.-T. Kim, *ACS Energy Lett.* **2017**, *2*, 1232.
[43] X.-B. Cheng, R. Zhang, C.-Z. Zhao, F. Wei, J.-G. Zhang, Q. Zhang, *Adv. Sci.* **2016**, *3*, 1500213.
[44] C. Yan, R. Xu, Y. Xiao, J.-F. Ding, L. Xu, B.-Q. Li, J.-Q. Huang, *Adv. Funct. Mater.* **2020**, *30*, 1909887.
[45] Y. Zhao, M. Amirmaleki, Q. Sun, C. Zhao, A. Codirenzi, L. V. Goncharova, C. Wang, K. Adair, X. Li, X. Yang, F. Zhao, R. Li, T. Filleter, M. Cai, X. Sun, *Matter* **2019**, *1*, 1215.
[46] J.-M. Kim, M. H. Engelhard, B. Lu, Y. Xu, S. Tan, B. E. Matthews, S. Tripathi, X. Cao, C. Niu, E. Hu, S.-M. Bak, C. Wang, Y. S. Meng, J.-G. Zhang, W. Xu, *Adv. Funct. Mater.* **2022**, *32*, 2207172.
[47] C. Wu, F. Guo, L. Zhuang, X. Ai, F. Zhong, H. Yang, J. Qian, *ACS Energy Lett.* **2020**, *5*, 1644.

[48] M. A. Weret, W.-N. Su, B. J. Hwang, *Batter. Supercaps* **2022**, *5*, e202200059.
[49] J. Conder, R. Bouchet, S. Trabesinger, C. Marino, L. Gubler, C. Villevieille, *Nat. Energy* **2017**, *2*, 17069.
[50] J. W. Dibden, J. W. Smith, N. Zhou, N. Garcia-Araez, J. R. Owen, *Chem. Commun.* **2016**, *52*, 12885.
[51] J. Yan, X. Liu, B. Li, *Adv. Sci.* **2016**, *3*, 1600101.
[52] F. Schmidt, S. Kirchhoff, K. Jägle, A. De, S. Ehrling, P. Härtel, S. Dörfler, T. Abendroth, B. Schumm, H. Althues, S. Kaskel, *ChemSusChem* **2022**, *15*, 202201320.
[53] L.-P. Hou, X.-Q. Zhang, B.-Q. Li, Q. Zhang, *Mater. Today* **2021**, *45*, 62.
[54] M. J. Lacey, A. Yalamanchili, J. Maibach, C. Tengstedt, K. Edström, D. Brandell, *RSC Adv.* **2016**, *6*, 3632.
[55] G. Rong, X. Zhang, W. Zhao, Y. Qiu, M. Liu, F. Ye, Y. Xu, J. Chen, Y. Hou, W. Li, W. Duan, Y. Zhang, *Adv. Mater.* **2017**, *29*, 1606187.
[56] J. Lopez, A. Pei, J. Y. Oh, G.-J. N. Wang, Y. Cui, Z. Bao, *J. Am. Chem. Soc.* **2018**, *140*, 11735.
[57] J. Zheng, Z. Ju, B. Zhang, J. Nai, T. Liu, Y. Liu, Q. Xie, W. Zhang, Y. Wang, X. Tao, *J. Mater. Chem. A* **2021**, *9*, 10251.
[58] J. Seo, W. Jeong, M. Lim, B. Choi, S. Park, Y. Jo, J.-W. Lee, H. Lee, *Energy Storage Mater.* **2023**, *60*, 102827.
[59] A. Rudawska, E. Jacniacka, *Int. J. Adhes. Adhes.* **2009**, *29*, 451.
[60] L. B. Freund, S. Suresh, *Thin Film Materials: Stress, Defect Formation and Surface Evolution,* Cambridge University Press, **2004**.
[61] B. Xu, Z. Liu, J. Li, X. Huang, B. Qie, T. Gong, L. Tan, X. Yang, D. Paley, M. Dontigny, K. Zaghib, X. Liao, Q. Cheng, H. Zhai, X. Chen, L.-Q. Chen, C.-W. Nan, Y.-H. Lin, Y. Yang, *Nano Energy* **2020**, *67*, 104242.
[62] Z. Liu, Y. Qi, Y. X. Lin, L. Chen, P. Lu, L. Q. Chen, *J. Electrochem. Soc.* **2016**, *163*, A592.
[63] Y. Yang, K. Y. Lee, X. F. Li, *Int. J. Fract.* **2018**, *210*, 81.
[64] K. Guo, P. A. Tamirisa, B. W. Sheldon, X. Xiao, H. Gao, *J. Electrochem. Soc.* **2018**, *165*, A618.
[65] H. Lee, D. J. Lee, Y.-J. Kim, J.-K. Park, H.-T. Kim, *J. Power Sources* **2015**, *284*, 103.
[66] E. Cha, H. Lee, W. Choi, *ChemElectroChem* **2020**, *7*, 890.
[67] H. Liu, X.-B. Cheng, R. Xu, X.-Q. Zhang, C. Yan, J.-Q. Huang, Q. Zhang, *Adv. Energy Mater.* **2019**, *9*, 1902254.
[68] F. Shi, A. Pei, D. T. Boyle, J. Xie, X. Yu, X. Zhang, Y. Cui, *Proc. Natl. Acad. Sci. U.S.A.* **2018**, *115*, 8529.
[69] X. Huang, Z. Wang, R. Knibbe, B. Luo, S. A. Ahad, D. Sun, L. Wang, *Energy Technol.* **2019**, *7*, 1801001.
[70] Y. Liu, H. Liu, Y. Lin, Y. Zhao, H. Yuan, Y. Su, J. Zhang, S. Ren, H. Fan, Y. Zhang, *Adv. Funct. Mater.* **2021**, *31*, 2104863.
[71] J. Zhou, T. Wu, Y. Pan, J. Zhu, X. Chen, C. Peng, C. Shu, L. Kong, W. Tang, S. L. Chou, *Adv. Funct. Mater.* **2022**, *32*, 2106966.
[72] A. L. Mong, Y. Ahn, R. Puttaswamy, D. Kim, *Energy Mater* **2023**, *3*, 300035.
[73] Y. Wang, D. Dang, M. Wang, X. Xiao, Y.-T. Cheng, *Appl. Phys. Lett.* **2019**, *115*, 043903.